Available online at www.CivileJournal.org

Civil Engineering Journal

(E-ISSN: 2476-3055; ISSN: 2676-6957)

Vol. 12, No. 02, February, 2026

A Correlated Random-Field Ising Model for Pore-Scale Hysteresis in Soil-Water Characteristic Curves

Angela Viviana Gómez Azuero [1*], Juan Carlos Salazar Montenegro [2]

[1] *Civil Engineering Program, Universidad Mariana, Pasto, Colombia.*

[2] *Department of Physics, Universidad de Nariño, Pasto, Colombia.*

Received 20 October 2025; Revised 14 January 2026; Accepted 19 January 2026; Published 01 February 2026

Abstract

The soil–water characteristic curve (SWCC) plays a central role in the behavior of unsaturated soils, yet explaining its hysteresis directly from pore-scale mechanisms remains challenging. The objective of this study is to investigate how pore-size heterogeneity, spatial correlations, and cooperative dynamics contribute to hysteresis in SWCCs. In this study, a correlated Random-Field Ising Model (RFIM) combined with Monte Carlo simulations is developed to represent the pore space as a two-dimensional lattice with a bimodal distribution of pore volumes and a spatially correlated disorder field. Drainage processes are simulated without parametric curve fitting, enabling direct analysis of pore-scale switching dynamics. The results show that macropore fraction, pore-size heterogeneity, and the activation parameter \beta exert a strong control on drainage behavior. Low \beta values produce smooth and nearly reversible drainage, whereas higher \beta stabilizes metastable pore configurations and yields abrupt transitions accompanied by hysteresis. The divergence between number-based and volume-based saturation serves as a useful indicator of size-selective drainage and cooperative pore-scale events. The novelty of this work lies in providing a physically grounded and statistically dynamics to macroscopic hysteresis in SWCCs, offering insights beyond traditional phenomenological or uncorrelated pore-network approaches.

Keywords: Soil–Water Characteristic Curve; Unsaturated Soils; Pore-Scale Modeling; Monte Carlo Simulation; Hysteresis; Microstructural Heterogeneity; Hydraulic Behavior; Pore Connectivity.

1. Introduction

The soil–water characteristic curve (SWCC) is a fundamental constitutive relation governing the behavior of unsaturated soils, underpinning predictions of hydraulic and mechanical processes in geotechnical and environmental applications [1, 2]. Accurate characterization of the SWCC is therefore essential for slope-stability assessment, foundation design, infiltration and drainage analyses, and coupled hydro-mechanical modeling [3–8]. Laboratory and field investigations have reaffirmed the central role of the SWCC while highlighting substantial variability in retention behavior across soil textures, densities, and structural states [9–11]. This variability underscores the need for models that relate measurable microstructural attributes—such as pore-size distribution, pore-size contrast, and connectivity—to macroscopic retention responses.

A central feature of the SWCC behavior is hysteresis, whereby drying and wetting paths do not coincide. The resulting hysteretic loop encodes information on metastability, ink-bottle effects, and path dependence within the pore network [12, 13]. Traditional parametric formulations provide compact and widely used representations of retention

* Corresponding author: avgomeza@umariana.edu.co

https://doi.org/10.28991/CEJ-2026-012-02-02

behavior, but they remain largely phenomenological, relying on fitting parameters without direct microstructural interpretation. These models reproduce observed curves but offer limited insight into the physical mechanisms that govern hysteresis.

Laboratory measurements and curve-fitting approaches remain essential for determining SWCCs [14, 15], but they are often limited in resolution, scalability, and coverage across the full suction range. Although indirect estimation methods and empirical correlations have been proposed to mitigate these limitations, their applicability across different textures, densities, and void-ratio conditions is not fully established [16, 17]. These challenges motivate the development of pore-scale models that can more explicitly link soil fabric to hydraulic response.

At the pore scale, hysteresis originates from multiple physical mechanisms—including ink-bottle effect, contact-angle hysteresis, and phase entrapment—each associated with the disordered geometry of natural porous media. Quantifying how these microscale features collectively generate macroscopic hysteretic loops remains an open challenge. Heterogeneity in pore sizes, shapes, and connectivity produces correlated fluctuations in local entry pressures and interfacial energies, yielding drainage and wetting pathways that cannot be captured by mean-field approaches or continuum descriptions alone. A physically grounded, statistically informed modeling framework is therefore needed to represent the interplay between disorder, local interactions, and cooperative dynamics. In this study, we focus on the conceptual mechanisms driving the retention response, rather than on predictive calibration, and examine how pore-scale disorder and local interactions shape the resulting hysteresis.

Recent numerical advances have addressed these challenges in part. Pore-network and lattice-based models have explored how pore geometry, coordination, and connectivity regulate capillary processes and hysteresis [18, 19]. High-resolution imaging combined with numerical homogenization and data-driven approaches [20, 21] has further improved the inference of hydraulic properties from microstructural information. Machine-learning approaches have also been applied to estimate SWCC parameters [22–25], offering predictive capability but often at the expense of physical interpretability. In parallel, recent studies have emphasized the strong influence of void ratio and fabric on the shape and position of the retention transition [26, 27].

Despite these advances, classical pore-network models are typically quasi-static and rely on deterministic entry-pressure rules, treating pore-scale disorder implicitly through prescribed geometrical thresholds. As a result, they are limited in their ability to represent metastable configurations, stochastic switching, and spatially correlated fluctuations in local entry potentials—features that are central to hysteresis and cooperative drainage behavior.

These limitations point to a broader gap in existing modeling approaches. Mean-field, curve-fitting and homogenized formulations capture average retention behavior but suppress spatial correlations and metastable pathways that govern hysteresis. Moreover, many pore-scale simulations track pore occupancy independently and not naturally yield interpretable macroscopic diagnostic—such as susceptibility peaks, differences between volumetric and numeric saturation, or indicators of cooperative response— that can be directly linked to microstructural organization. Together, these constraints highlight the absence of a pore-scale, probabilistic, and physically interpretable framework capable of capturing cooperative dynamics in soil–water retention.

Statistical physics provides promising tools to address this gap [28–30]. In particular, the Random-Field Ising Model (RFIM) provides an energy-based, probabilistic framework in which disorder, neighbor interactions, and external driving are treated on equal footing. Originally developed to describe cooperative transitions and hysteresis in disordered systems [31–34], the RFIM naturally incorporates spatial correlations and metastability, making it well suited to represent collective pore-scale processes. When adapted to unsaturated porous media, correlated random-field formulations enable hysteresis and cooperative drainage to emerge as intrinsic system responses, rather than as imposed invasion rules.

This study addresses these challenges through a correlated RFIM implemented using Monte Carlo simulations. Building on earlier statistical-mechanics formulations [30–35], the proposed approach departs from mean-field closure and explicitly resolves the spatial evolution of pore occupancy under imposed matric potential. Monte Carlo sampling enables exploration of metastable configurations and cooperative switching events, while the local suction field combines a pore-volume dependence with a correlated random component representing intrinsic heterogeneity. This formulation allows systematic investigation of how volume contrast and macropore content regulate macroscopic hysteresis.

The proposed framework links microstructural descriptors to interpretable macroscopic diagnostics, including volume-weighted versus number-weighted saturation and regimes of cooperative drainage, without reliance on empirical curve fitting. By resolving spatial correlations and stochastic dynamics, the model provides a physically grounded characterization of pore-scale mechanisms underlying SWCC hysteresis and offers a pathway toward interpretable, pore-informed descriptions relevant to experimental analysis and reduced-order modeling.

The remainder of the paper is organized as follows. Section 2 presents the overall methodology. Section 3 details the pore-network formulation and RFIM implementation. Section 4 reports the results and analysis of cooperative drainage behavior. Section 5 summarizes the main conclusions and outlines directions for future work.

2. Research Methodology

This study develops a pore-scale modeling approach to examine the SWCC and its hysteretic behavior by combining concepts from statistical physics with stochastic lattice simulations. The objective is to relate microscopic pore structure to macroscopic hydraulic response. Figure 1 summarizes the main stages of the workflow, from pore-network generation to simulation and analysis.

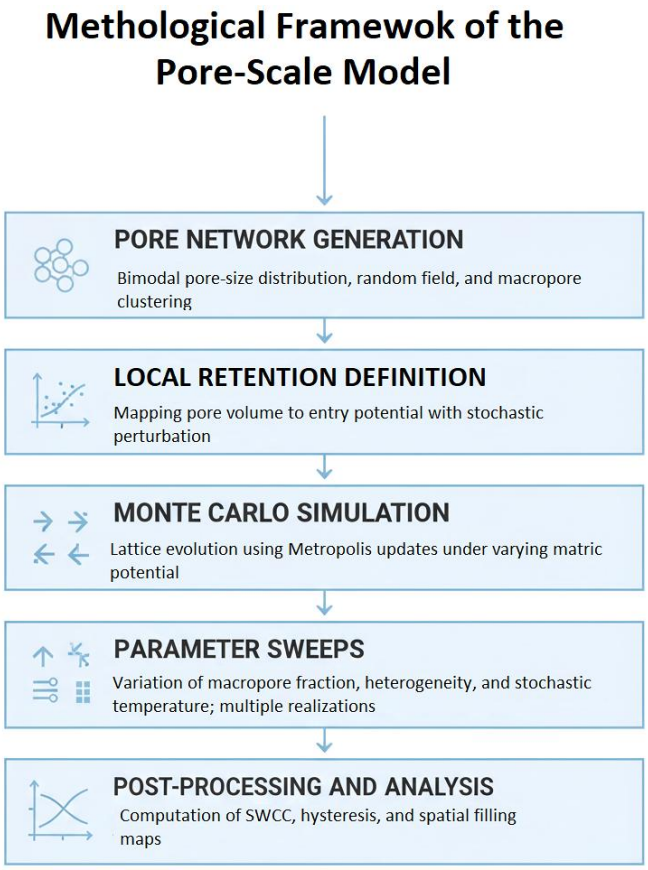

Figure 1. Research flowchart

2.1. Conceptual Basis of Hysteresis

The modeling framework is grounded on established pore-scale mechanisms associated with hysteresis in unsaturated soils, including the ink-bottle effect, contact-angle variability, and metastable interface behavior [36–39]. This mechanisms motivate representing retention as the outcome of local interactions within a disordered pore network.

2.2. Construction of Synthetic Pore Networks

The pore structure was represented on a two-dimensional lattice approximating the void arrangement of a granular medium [40, 41]. Pore volumes were drawn from a bimodal probability distribution [42–45] to control the relative abundance of micro- and macropores. Spatial correlations were introduced by smoothing an underlying random field and applying a threshold to identify contiguous macropore regions.

2.3. Local Retention Field

Each lattice site was assigned a local entry potential derived from its pore volume, following a monotonic scaling between pore size and capillary pressure. A correlated random component was added to represent intrinsic irregularities such as surface roughness or throat variability. The resulting random field, combining deterministic and stochastic elements, reflects both structural heterogeneity and quenched disorder typical of natural porous media.

2.4. Monte Carlo Simulation of Drainage

The temporal evolution of the pore system was modeled using a Monte Carlo algorithm with a Metropolis acceptance criterion [46]. Each pore could be either water-filled or air-filled, and transition probabilities depended on the imposed matric potential and the states of neighboring sites, representing capillary coupling and cooperative effects. The external potential was varied gradually to reproduce drainage behavior.

2.5. Parameter Exploration and Averaging

A systematic exploration of model parameters was performed to assess the influence of macropore fraction, pore-size contrast, correlation length, and stochastic temperature. Multiple realizations of the correlated field were generated for each parameter set to separate systematic trends from random fluctuations.

2.6. Data Processing and Analysis

Two complementary saturation measures were computed from each simulation: number-weighted saturation (fraction of filled pores) and volume-weighted saturation (fraction of total pore volume filled). Their divergence indicates the presence of cooperative filling and heterogeneity-driven transitions. Additional quantities—such as hysteresis curves, and spatial filling patterns—were extracted to characterize microstructural evolution.

3. Pore-Network Model Formulation

The present model extends the lattice-based framework introduced by Gómez [35] by incorporating a volume-weighted formulation of saturation and an explicit representation of a bimodal pore-size distribution. Micropores and macropores are assigned distinct volume classes, producing spatially distributed heterogeneity representative of dual-porosity soils..

The model is designed to reproduce the hysteretic behavior typically observed in SWCCs of unsaturated soils. Conventional pore-network or lattice-based approaches often estimate the degree of saturation as a direct function of pore occupancy or average pore state, overlooking the variability in pore sizes that governs water retention and phase-transition dynamics. By explicitly incorporating the distribution of pore volumes, the model captures the differential influence of micro- and macropores: larger pores contribute more to the overall saturation, while smaller pores retain their capillary effect. This yields a physically coherent description of the soil microstructure and its macroscopic hydraulic response.

The porous medium is represented as a two-dimensional lattice of interconnected pores, each of which can exist in a filled or empty state. Transitions between these states depend on energy variations arising from interfacial forces, neighbor interactions, and the applied suction. By accounting for these mechanisms, the formulation connects the dynamics of individual pores with the macroscopic hysteresis observed in SWCCs.

The following section describes the energetic basis of the model, including the contributions to the total energy change associated with pore transitions and the variables used to determine equilibrium configurations.

3.1. Conceptual Representation of the Pore Lattice

The soil's void space is represented as a two-dimensional lattice of interconnected pores, providing a simplified yet physically meaningful framework to analyze water retention and hysteresis. Each lattice site (i, j) corresponds to a single pore that can exist in one of two states: water-filled ($\sigma_{ij} = +1$) or air-filled ($\sigma_{ij} = -1$). Pores are connected through throats that enable capillary interaction between neighboring sites. The coordination number, defined as the number of directly connected neighbors, explicitly influences the degree of local connectivity and cooperative behavior within the lattice.

Although the representation is two-dimensional, it captures the essential cooperative features of drainage–imbibition processes that also arise in three-dimensional pore networks, as demonstrated in previous pore-network studies [18, 47]. In three dimensions, higher coordination numbers and additional invasion pathways are expected to modify percolation thresholds, cluster morphology, and the sharpness of cooperative transitions. However, the underlying mechanisms governing metastability, collective pore switching, and hysteresis—namely the interplay between disorder, local interactions, and external driving—are not dimensional artifacts and persist across lattice dimensionality. The two-dimensional approximation therefore provides a controlled framework to isolate and analyze these mechanisms while acknowledging that quantitative thresholds and cluster geometries would shift in three-dimensional extensions.

To represent the intrinsic heterogeneity of natural soils, pore volumes ($V_{p,i}$) are assigned according to a bimodal probability distribution, distinguishing between micro- and macropores. Larger pores contribute more significantly to volumetric saturation, while smaller pores retain capillary water at lower matric potentials—consistent with experimental evidence in unsaturated soils. This bimodal assignment introduces spatial variability that shapes local clusters and affects the energy landscape governing pore transitions.

This conceptualization provides a flexible and physically grounded foundation for the subsequent energetic formulation and Monte Carlo simulations. It allows for systematic exploration of how pore-size heterogeneity, network connectivity, and external suction (ψ') interact to produce the observed SWCC hysteresis

Figure 2 provides a schematic overview of the two-dimensional pore-network representation adopted in this study, illustrating pore states, connectivity, and local interactions that govern energy transitions. Blue and white circles denote water- and air-filled pores, respectively. Circle size reflects pore volume, while gray lines represent throats connecting neighboring pores. Shaded regions highlight clusters of uniform state, and a red outline marks a selected pore and its neighbors, illustrating the local interactions that determine energy transitions within the lattice.

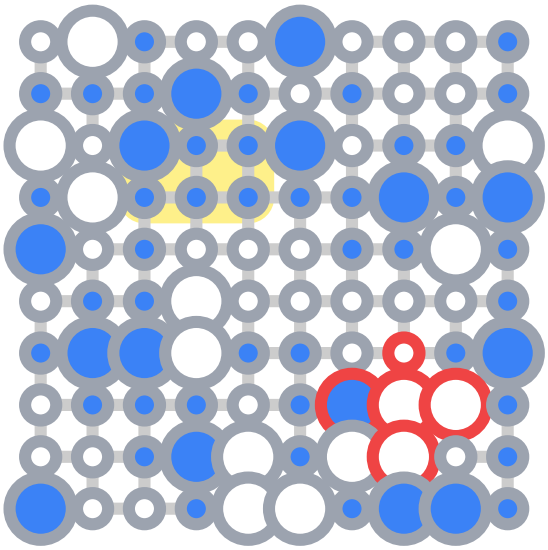

Figure 2. Schematic representation of the 2D pore network used in the model

The following section formalizes the energetic contributions from water–air and solid–water interfaces, as well as the work associated with externally applied suction, establishing a mechanistic link between the microscopic lattice configuration and the macroscopic hysteresis observed in the SWCC.

3.2. Energy Changes Associated with Pore Transitions

The energetic formulation builds upon established pore-scale models for capillary hysteresis [30, 35], extended here to include volume-weighted pore contributions and bimodal pore-size distributions. These additions yield a physically consistent description suitable for Monte Carlo simulations of hysteresis in the SWCC.

Energy variations associated with pore transitions describe the filling and emptying dynamics within the lattice. For a pore located at site (i,j), initially water-filled ($\sigma_{ij} = +1$), the total energy required to switch it to an air-filled state ($\sigma_{ij} = -1$) is expressed as

$$\Delta E_{ij} = \Delta E_{wa} + \Delta E_s + W_\psi, \quad (1)$$

where, ΔE_{wa} denotes the change in water–air interfacial energy, ΔE_s represents the change in solid–fluid interfacial energy associated with the pore walls, and W_ψ accounts for the energetic contribution arising from the externally applied suction field.

The water–air interfacial term depends on the occupancy of neighboring pores. When a pore empties, interfaces shared with adjacent water-filled neighbors are removed, whereas interfaces with air-filled neighbors may be created. This contribution can be compactly expressed as

$$\Delta E_{wa} = \sum_{(k,l)\in N_{ij}} \sigma\left(\sigma_{ij}, \sigma_{kl}\right) \gamma_{wa}\, a_{t,(ij)\leftrightarrow(kl)}, \quad (2)$$

where, N_{ij} is the set of neighbors of site (i,j), $a_{t,(ij)\leftrightarrow(kl)}$ is the throat area between pores (i,j), (k,l) , and γ_{wa} is the water–air interfacial tension [N/m]. The sign function $\sigma\left(\sigma_{ij}, \sigma_{kl}\right)$ distinguishes between interface creation (positive) and removal (negative)..

The solid–fluid term is given by;

$$\Delta E_s = (\gamma_{sa} - \gamma_{sw}) A_p, \quad (3)$$

where, A_p is the internal surface area of the pore walls, and γ_{sw} and γ_{sa} are the solid–water and solid–air interfacial energies, respectively. This term accounts for wettability effects arising when the pore surface transitions from a water-wet to an air-wet state.

The suction contribution is represented through a local potential expressed in units of energy [J] for dimensional consistency within the Hamiltonian. Because the externally imposed matric potential ψ' has units of pressure [Pa], conversion to energy is achieved by multiplying by a reference volume $V_0 = \langle V_p \rangle$, where $\langle V_p \rangle$ de denotes the mean pore volume of the lattice, taken as $1 \times 10^{-10}\ m^3$. Defining a characteristic energy $E_0 = p_{\text{ref}} V_0 = 1 \times 10^{-6}$ J with $p_{\text{ref}} = 10^4$ Pa, the local potential is:

$$W_\psi = \psi' V_0 \left(\frac{V_{p,i}}{V_0}\right)^\alpha + h_i, \quad (4)$$

where, $V_{p,i}$ is the volume of pore i, $\alpha = -1/3$ follows the Young–Laplace scaling for capillary entry pressure, and h_i represents a quenched random field that accounts for local geometric and connectivity disorder.

The normalized potential ($\tilde{\psi}_i$) is then:

$$\tilde{\psi}_i = \frac{\psi'}{p_{\text{ref}}} \left(\frac{V_{p,i}}{V_0}\right)^\alpha + \frac{h_i}{E_0}. \quad (5)$$

Evaluating ΔE_{ij} for all pores captures both cooperative (neighbor-mediated) and stochastic effects in water redistribution, establishing a direct physical link between pore-scale energetics and macroscopic hysteresis in the SWCC. This formulation provides a rigorous foundation for Monte Carlo simulations of unsaturated soil behavior.

3.3. Random-Field Ising Model Implementation

Following the energetic framework introduced earlier, the system is implemented as a correlated Random-Field Ising Model (RFIM), for which the total energy of the system, or Hamiltonian, is expressed as:

$$H = -\sum_{(i,j)} \sum_{(k,l)\in N_{ij}} J_{(i,j),(k,l)}\, \sigma_{ij}\, \sigma_{kl} - \sum_{(i,j)} \psi_i\, \sigma_{ij}, \quad (6)$$

where, $J_{(i,j),(k,l)}$ denotes the coupling strength between adjacent pores, reflecting the geometric and interfacial characteristics of the connecting throat, while the second term represents the local suction bias acting on each pore through the potential ψ_i.

This Hamiltonian explicitly incorporates cooperative interactions (first term) and quenched heterogeneity (second term), allowing the RFIM framework to represent how applied suction, pore geometry, and structural disorder jointly control retention and hysteresis in the SWCC.

For clarity, the sign convention for J is chosen such that positive values favor like-state alignment, corresponding to water–water or air–air configurations.

In the numerical implementation, the water–air interfacial contribution described in Section 3.2 is represented implicitly through the effective coupling parameter J, which aggregates geometric and interfacial effects of the connecting throats.. For simplicity, $J$was normalized to unity ($J = 1$) to define the reference energy scale in the simulations.

The corresponding physical scaling can be recovered from the approximate relation $\gamma_{wa}\, a_{t,(ij)\leftrightarrow(kl)} \approx J\, E_0$, where $E_0 = p_{\text{ref}} V_0$ is the reference energy.

3.4. Monte Carlo Simulation Framework

Equilibrium and metastable lattice configurations under prescribed suction are obtained using a Metropolis–Hastings Monte Carlo (MC) algorithm that samples configurations according to the Boltzmann probability exp $(-\beta H)$.

The energy difference associated with flipping a single spin at site (i, j) is;

$$\Delta E_{ij} = 2\, \sigma_{ij} \left(\sum_{(k,l)\in N_{ij}} J_{(i,j),(k,l)}\, \sigma_{kl} + \psi_i\right), \quad (7)$$

where the factor of 2 arises from the symmetric energy difference between the two states ($\sigma_{ij} \to -\sigma_{ij}$).

The proposed flip is accepted with probability

$$P_{\text{accept}} = \min(1,\, e^{-\beta \Delta E_{ij}}), \quad (8)$$

Here, β is best understood as an effective activation parameter rather than a physical temperature in the thermodynamic sense. In real unsaturated soils, drainage and imbibition occur under essentially athermal conditions; thermal fluctuations at ambient temperatures are negligible compared to capillary energy barriers. Consequently, β does not correspond to a measurable soil temperature or material constant.

Instead, β provides a numerical and conceptual control parameter that regulates the relative importance of energetic barriers versus stochastic switching in the pore-scale dynamics. Low β values allow frequent activated events and smooth, nearly reversible transitions, while high β values suppress fluctuations, stabilize metastable configurations, and promote abrupt, hysteretic drainage. In this sense, β plays a role analogous to an activation scale reflecting unresolved sources of variability in real soils, such as local geometric irregularities, surface roughness, contact-angle variability, or microscale hydraulic perturbations. Therefore, β should be interpreted as a phenomenological parameter that enables systematic exploration of metastability and cooperative effects, rather than as a direct physical property of the soil.

The simulation protocol consists of two stages:

- ***Equilibration*:** The lattice is initialized in a prescribed configuration (fully saturated for drainage or fully dry for imbibition) and evolved through successive MC sweeps until macroscopic observables reach a quasi-stationary regime.
- ***Production*:** Once equilibration is achieved, additional MC sweeps are performed to sample configurations and compute ensemble-averaged quantities.

Two measures of water saturation are evaluated. The number-based saturation (S_{num}) is defined as

$$S_{\mathrm{num}} = \frac{\langle \sigma_{ij} \rangle + 1}{2}, \tag{9}$$

where, $\langle \cdot \rangle$ denotes the lattice average.

The volume-weighted saturation ($S_{\mathrm{vol}}(\psi')$) explicitly accounts for pore-size heterogeneity:

$$S_{\mathrm{vol}}(\psi') = \frac{\sum_{(i,j)} V_{p,i}\, \phi_{ij}(\psi')}{\sum_{(i,j)} V_{p,i}}, \qquad \phi_{ij}(\psi') = \frac{\sigma_{ij}+1}{2}\, w_{ij}, \qquad w_{ij} = \frac{V_{p,i}^{\alpha}}{\langle V_p^{\alpha} \rangle}, \tag{10}$$

where, $\phi_{ij}(\psi')$ is an occupation indicator equal to 1 for a water-filled pore and 0 for an air-filled pore, w_{ij} is a weighting factor that accounts for pore-size effects through a normalized volume-dependent term, and $\langle V_p^{\alpha} \rangle$ denotes the lattice average of $V_{p,i}^{\alpha}$. This formulation ensures that macropores and micropores contribute proportionally to their volumetric weights, allowing the results to be expressed in the same form as experimental SWCC data, which are typically reported in volumetric terms. By gradually sweeping ψ' and recording both S_{vol} and S_{num} along drainage and imbibition paths, the model reproduces hysteretic soil–water characteristic curves and clarifies the influence of coupling strength, pore-size bimodality, and structural disorder in shaping the hydraulic response.

The main simulation parameters and numerical settings are summarized below to ensure reproducibility and dimensional consistency. All simulations were performed on square lattices of size 128 × 128, providing a balance between spatial representativeness and computational efficiency. Each parameter combination was averaged over 20 independent realizations of the quenched disorder field to ensure statistical robustness.

The random field $h_i$was generated as a spatially correlated Gaussian field by smoothing an initially uncorrelated white-noise field with a Gaussian kernel. This procedure produces an isotropic, zero-mean field with approximate covariance $C(r) \propto \exp\left[-(r/\xi)^2\right]$, where the correlation length ξ (proportional to the smoothing width) ranged from 2 to 10 lattice units.

This range was selected to systematically span regimes from weakly correlated disorder, where heterogeneity is essentially local, to strongly correlated disorder characterized by mesoscopic domains of similar pore properties. In the context of real soils, the correlation length can be interpreted as a statistical proxy for structural features such as aggregate size, clustered macropore regions, or spatial persistence in pore connectivity, rather than as a direct physical length scale. The chosen values therefore represent plausible orders of magnitude for correlated soil fabric heterogeneity while avoiding system-size effects.

The standard deviation of the disorder field was set to $\sigma_h = 0.05\, E_0$, representing moderate heterogeneity typical of natural granular materials. The field h_i was treated as quenched (fixed for each realization), representing intrinsic structural heterogeneity rather than dynamic fluctuations.

Each simulation comprised 5×10^4 equilibration sweeps followed by 1×10^5 production sweeps. These values were selected based on preliminary convergence tests in whichthe temporal evolution of the total energy and the volume-weighted saturation S_{vol} was monitored for representative combinations of disorder strength, correlation length, and interaction parameters, For all tested cases, equilibration was reached within approximately 1×10^4 sweeps, after which macroscopic observables fluctuated around stationary mean values.

The adopted equilibration and production lengths therefore provide a conservative margin ensuring stable time-averaged quantities. Convergence was verified through the temporal stability of both the total energy and S_{vol}, with variations below 0.5% over successive sampling windows. Statistical convergence was further confirmed by comparing ensemble-averaged observables across independent disorder realizations, which differed by less than 0.5%.

Parameter combinations associated with strong disorder or pronounced cooperative drainage—where metastable configurations persist longer—exhibited slower relaxation but did not require qualitatively different sweep counts; increasing equilibration or production lengths by a factor of two in selected cases resulted in changes below 1% in the computed SWCCs. Tests performed on larger lattices (256 × 256) likewise produced negligible differences (<1%), confirming that finite-size effects are minimal and that the adopted simulation protocol ensures both accuracy and computational efficiency.

4. Results: Linking Pore-Scale Disorder to Macroscopic Hysteresis

This section presents the outcomes of the correlated RFIM simulations and demonstrates how pore-scale heterogeneity, pore-size contrast, and local interactions jointly determine the macroscopic form of the SWCC. The analysis progressively connects statistical and spatial descriptors of the pore architecture with the emergence of cooperative dynamics and hysteresis during drainage.

4.1. Statistical Characterization of the Pore Structure

The synthetic pore network used in the RFIM simulations exhibits pronounced spatial and statistical heterogeneity, providing the microstructural basis for the cooperative drainage behavior analyzed in later sections. Figure 3 summarizes the structural features of the 128×128 lattice. Panel (a) displays the spatial distribution of normalized pore volumes $V_{p,i}/\langle V_p \rangle$, revealing a heterogeneous medium composed of clustered macropores embedded in a fine microporous matrix. This multiscale arrangement—characteristic of aggregated and biogenically structured soils—gives rise to local contrasts in entry pressures and stability, which are explicitly incorporated into the random-field term of the RFIM formulation.

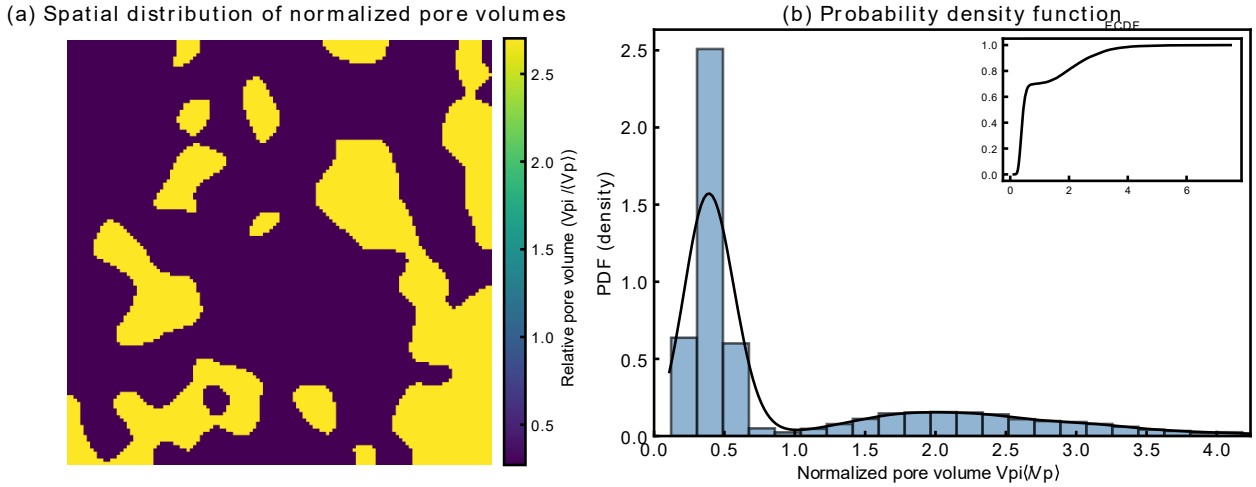

Figure 3. (a) Spatial distribution of normalized pore volumes ($V_{p,i}/\langle V_p \rangle$) on a 128×128 lattice, showing a heterogeneous medium with clustered macropores surrounded by a microporous matrix. (b) Probability density function (PDF) of normalized pore volumes, showing a strongly right-skewed bimodal distribution.

The pore-size distribution used to generate this lattice is shown in Figure 3-b. The probability density function (PDF) is markedly right-skewed, with a dominant peak in the micropore range. The statistical asymmetry is quantified by a positive skewness of approximately 0.87, reflecting the long tail associated with large macropores. The fourth central moment (kurtosis) is about 1.76, which is lower than the Gaussian kurtosis (3.0); this reduction is consistent with the bimodal character of the distribution, as two separated modes tend to yield a lower global kurtosis than a single, sharply peaked distribution.

The empirical cumulative distribution function (ECDF) further illustrates this imbalance: approximately 70% of the pores exhibit volumes below the mean, while a numerically sparse subset—only about 30% of all pores—accounts for nearly 79% of the total pore volume. This volumetric dominance of macropores explains why the volume-weighted saturation departs markedly from the number-weighted saturation in the transition region of the SWCC

Empirical and imaging studies indicate that pore-size distributions of this type are representative of aggregated and structured soils, where macropores constitute a numerically minor but volumetrically dominant fraction of the pore space. Micro–computed tomography (micro-CT) and mercury intrusion porosimetry (MIP) analyses commonly report macropore volume fractions on the order of 5–30% of the total porosity, together with macropore–micropore size contrasts spanning one to two orders of magnitude, depending on texture and aggregation state [47]. The statistical characteristics of the synthetic lattice shown in Fig. 3—including the strong right-skewness of the pore-size distribution and the volumetric dominance of a sparse macropore population—therefore fall within experimentally reported regimes and provide a realistic microstructural basis for examining cooperative drainage and hysteresis.

4.2. Soil–Water Characteristic Curves Derived from the RFIM

The evolution of saturation under increasing or decreasing matric potential is examined through the SWCCs generated by the correlated RFIM. These curves reflect how pore-scale heterogeneity, cooperative interactions, and stochastic fluctuations jointly determine macroscopic water retention. Figures 4-a to 4-c summarize the response for different values of β and two pore–suction scaling exponents.

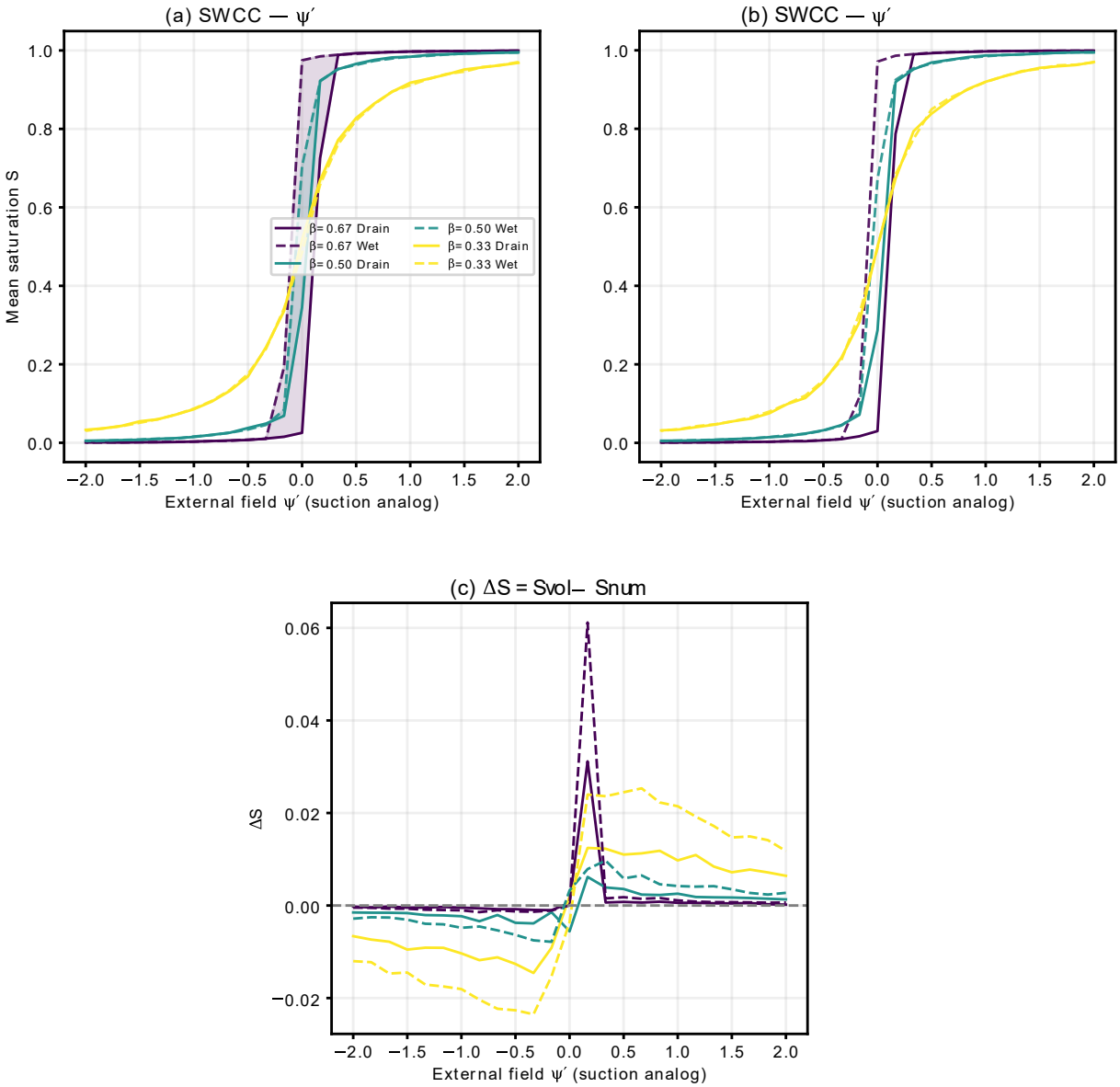

Figure 4. SWCCs derived from the correlated RFIM. (a) SWCCs for $\alpha = -1/3$, showing the shift from smooth, nearly reversible behavior at low β (0.33) to a sharp, hysteretic transition at higher β (0.50 − 0.67). (b) SWCCs for $\alpha = -1/2$. (c) Difference between volume- and number-weighted saturations ($\Delta S = S_{vol} - S_{num}$) versus ψ'.

In this formulation, the external field ψ' acts as an analog of the matric suction applied to the system. Increasing ψ' corresponds to drainage, whereas decreasing ψ' corresponds to wetting. The parameter β regulates the balance between stochastic fluctuations and energetic constraints: low β emulates highly mobile capillary interfaces with frequent local switches, while high β suppresses fluctuations and promotes metastable configurations that give rise to hysteresis. This interpretation is consistent with the RFIM, where β controls the ability of the system to cross local energy barriers.

Figure 4-a presents the SWCCs obtained when $\alpha = -1/3$, which corresponds to the classical spherical-pore approximation. The curves reveal a clear progression with β. For $\beta = 0.33$, desaturation is smooth and nearly reversible, indicating that fluctuations dominate over cooperative effects. As β increases ($\beta = 0.50 - 0.67$), the transition region steepens and distinct drainage and wetting branches emerge. The growing hysteresis loop reflects the stabilization of metastable configurations and cooperative filling events, consistent with the increased rigidity of capillary interfaces at high β.

Similar trends have been reported in pore-network and experimental studies of unsaturated soils, where increased connectivity and reduced interfacial mobility lead to steeper retention transitions and wider hysteresis loops [48]. In classical pore-network models, this behavior is typically attributed to invasion sequences controlled by pore-throat geometry, whereas in the present RFIM formulation it emerges naturally from the competition between disorder, neighbor interactions, and metastability. This distinction highlights the ability of the RFIM to reproduce SWCC hysteresis as an emergent collective phenomenon rather than as a prescribed invasion rule.

Figure 4-b compares the SWCCs obtained using a stronger pore-volume dependence, $\alpha = -1/2$. A larger exponent amplifies the contrast between fine and coarse pores, producing a slightly sharper transition and shifting the drainage threshold toward higher ψ'. This behavior mimics soils with pronounced constrictions or ink-bottle geometries, in which macropores empty rapidly while micropores remain water-filled until substantially larger suction levels. The RFIM thus captures how pore-size distribution and connectivity shape the emergent SWCC without requiring empirical fitting.

Figure 4-c shows the difference $\Delta S = S_{vol} - S_{num}$ for the same parameter sets. At low β, $\Delta S \approx 0$ across the ψ' range, indicating that all pores contribute similarly to saturation. As β increases, a pronounced positive peak appears near the transition region. This arises because macropores—although few in number—dominate the total pore volume and therefore drain first, generating a drop in S_{vol} while S_{num} remains high due to water retained in the numerous micropores. This divergence is a direct signature of cooperative filling dynamics and spatial heterogeneity, and cannot be reproduced by independent-pore models.

The emergence of a well-defined peak in ΔS near the retention transition indicates that macroscopic hysteresis is closely tied to selective, collective drainage of volumetrically dominant pores. This behavior is consistent with imaging and pore-scale studies showing that early drainage is governed by connected macropore domains, while the fine pore matrix remains largely saturated [49]. By explicitly resolving the divergence between volumetric and numeric saturation, the RFIM provides a diagnostic that links pore-scale heterogeneity to macroscopic retention behavior in a way that is not accessible through independent-pore or purely empirical SWCC models.

Therefore, the correlated RFIM reproduces essential features of experimental SWCCs: smooth and reversible behavior under high disorder, steep transitions and hysteresis under low disorder, dependence on pore-scale geometry, and divergence between volumetric and numerical saturation. The correspondence between β and the degree of metastability parallels the transition between thermally activated and a thermal regimes in disordered materials. These emergent curves form the basis for the spatial and cooperative analyses presented in subsequent sections.

4.3. Effect of Pore-Scale Heterogeneity on Cooperative Dynamics

To quantify how microstructural heterogeneity fosters collective pore switching, we compute the maximum magnitude of the difference between the volume-weighted and number-weighted saturations ($|\Delta S|_{\max}$) across the desaturation sweep:

$$|\Delta S|_{\max} = \max_{\psi'} = |S_{vol} - S_{num}|, \tag{11}$$

and map this metric as a function of the macropore fraction (vertical axis) and the logarithm of the pore-volume contrast (horizontal axis). This measure captures the strongest size-selective response of the network—i.e., the point where the contributions of large and small pores to saturation diverge most—and therefore serves as an operational proxy for cooperative heterogeneity in the correlated RFIM.

Figure 5 shows the resulting contour map for a representative value of the interaction parameter in the cooperative regime ($\beta = 0.67$). The pore-volume contrast is reported as the base-10 logarithm of the ratio between the characteristic macropore and micropore volumes used to generate the bimodal distribution. The color scale indicates the magnitude of $|\Delta S|_{\max}$: bright (yellow) regions correspond to strong cooperative effects, whereas dark (purple) regions indicate nearly homogeneous behavior.

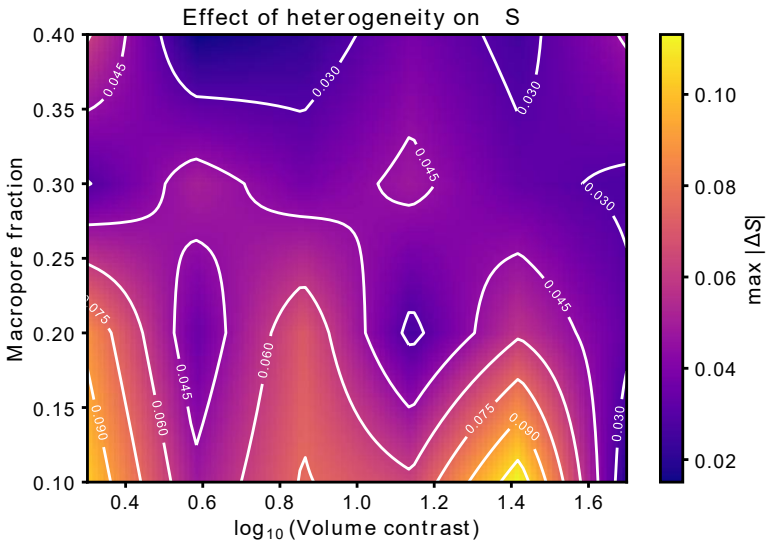

Figure 5. Contour map of the maximum divergence between volume- and number-weighted saturations, $|\Delta S|_{\max}$, as a function of macropore fraction and pore-volume contrast (β = 0.67)

An important observation is that the largest cooperative effects do not occur at the highest macropore fractions. Instead, $|\Delta S|_{\max}$ reaches its maximum for intermediate macropore contents ($\approx 0.12 - 0.22$), particularly when combined with large volume contrasts (log_{10} contrast $\approx 1.3 - 1.5$). In this regime, macropores are sufficiently abundant to interact and drain cooperatively, yet still sparse enough to remain volumetrically dominant. This combination causes macropores to empty abruptly while the numerous micropores remain water-filled, producing a pronounced divergence between volume-weighted and number-weighted saturation.

This regime corresponds to a cooperative drainage mechanism in which connected macropores empty through correlated switching events rather than independent invasion. Similar behavior has been reported in pore-network and imaging-based studies of structured soils, where drainage proceeds through preferential emptying of connected macropore domains while the fine matrix remains largely saturated [50, 51]. In contrast to classical pore-network models, which typically describe this process qualitatively through invasion sequences, the present RFIM framework captures this behavior through an explicit macroscopic indicator ($|\Delta S|_{max}$) that reflects the collective response of the pore network and its metastable configurations.

When the macropore fraction becomes too large (> 0.30), the medium behaves effectively homogeneous: macropores drain nearly synchronously, micropores contribute little to the total pore volume, and $|\Delta S|_{\max}$ decreases toward zero. Conversely, when macropores are too scarce (< 0.10), their spatial isolation prevents collective domain formation, and cooperative effects remain weak.

The emergence of a well-defined ridge of high $|\Delta S|_{max}$ in Figure 5 further suggests that macroscopic hysteresis is not solely controlled by local pore-scale thresholds, but by the interplay between pore-size contrast, spatial connectivity, and cooperative dynamics [52–54]. This observation is consistent with statistical-mechanics studies of disordered capillary systems, in which hysteresis arises from metastable states and avalanche-like transitions rather than smooth, reversible drainage [55, 56]. The present results therefore provide a quantitative link between microstructural heterogeneity and the collective mechanisms underlying SWCC hysteresis.

The contour map in Figure 5 thus provides a practical guide for identifying the structural conditions under which pore-scale heterogeneity produces strong size-selective desaturation (large $|\Delta S|$) and associated macroscopic hysteresis. Soils or materials containing sparse but volumetrically dominant macropores—especially under high contrast—are most likely to exhibit abrupt drainage events and strong divergences between volumetric and numeric saturation. Conversely, systems with either low contrast or very high macropore fractions respond more uniformly. This insight is valuable for experimental design: imaging or SWCC measurements targeted at the ridge region should capture cooperative avalanching and pronounced deviations between S_{vol} and S_{num}. In this sense, the present RFIM framework complements pore-network and imaging-based studies by providing explicit macroscopic diagnostics that quantify cooperative drainage and metastability, rather than inferring them indirectly from invasion sequences [18].

4.4. Microstructural Evolution during Drainage

The macroscopic hysteresis and cooperative effects identified in the previous sections originate from the reorganization of pore-scale filling patterns during drainage. Understanding this microstructural evolution is essential for connecting the emergent behavior of the correlated RFIM to physically meaningful capillary processes.

To visualize these mechanisms directly, we examine the spatial configuration of water- and air-filled pores across representative values of the imposed matric potential ψ'. Figure 6 shows the corresponding microstructural states, highlighting how wet and dry domains reorganize as the system evolves from saturation toward the dry regime. . Each circle corresponds to an individual pore site in the simulated two-dimensional lattice, and its color indicates the local filling state: blue sites are water-filled, while white sites denote air-filled pores. The three panels correspond to (a) a fully saturated state, (b) the transition region, and (c) an almost dry configuration.

At $\psi' = -2.0$ the system remains almost completely saturated, with nearly all pores filled with water. Only a few isolated air-filled sites appear, corresponding to the largest macropores that drain first due to their lower capillary entry pressures. The microstructure is therefore highly correlated and dominated by a continuous water domain spanning most of the lattice, consistent with the left portion of the SWCCs in Figure 4.

As ψ' increases toward the transition region ($\psi' = 0$), drainage proceeds in a heterogeneous and spatially clustered manner. Air-filled pores begin to nucleate preferentially within regions associated with macropores and then expand into neighboring pores. The coexistence of water and air clusters reflects the onset of cooperative interactions: once a small patch drains, the local field acting on adjacent pores shifts, lowering the energetic barrier for their drainage.

By $\psi' = 2.0$, the system approaches the dry state. Most pores are drained, and only small, isolated water clusters remain. These trapped clusters arise due to local geometric constraints and the stabilizing effect of neighboring drained pores, which impose energy barriers against further desaturation.

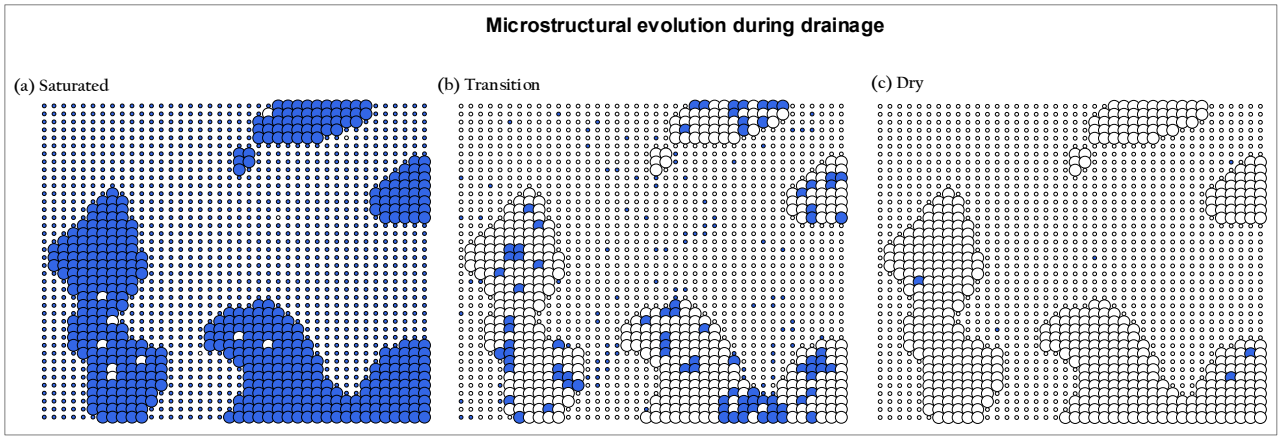

Figure 6. Microstructural evolution during drainage. Pore-filling configurations at (a) $\psi' = -2.0$, (b) 0, and (c) 2.0. Blue circles represent water-filled pores and white circles drained ones. Drainage evolves from a nearly saturated state to heterogeneous air-cluster formation and finally to a mostly dry network with trapped water pockets. This sequence highlights cooperative interactions and the origin of hysteresis in the SWCCs.

The microstructural snapshots reveal the internal pathway that underlies the macroscopic hysteresis observed in the SWCCs. The correlated RFIM captures the transition from smooth, reversible behavior at high disorder to irreversible drainage dominated by cooperative, avalanche-like events.

5. Conclusion

This study demonstrates that pore-scale heterogeneity, spatially correlated disorder, and cooperative interactions jointly govern drainage behavior and hysteresis in unsaturated porous media. Using a correlated Random-Field Ising Model (RFIM) combined with Monte Carlo dynamics, the proposed framework establishes a physically interpretable link between microstructural attributes and macroscopic soil–water characteristic curves (SWCCs). The activation parameter β plays a central role in controlling metastability: low β values promote smooth and nearly reversible desaturation dominated by stochastic fluctuations, whereas higher β suppress local fluctuations, stabilize metastable pore configurations, and lead to abrupt transitions accompanied by pronounced hysteresis. The explicit incorporation of a bimodal pore-size distribution further reveals how pore-size contrast and spatial clustering regulate cooperative drainage processes.

The analysis highlights the divergence between volume-weighted and number-weighted saturation (ΔS), which emerges as a robust quantitative indicator of size-selective drainage and collective pore switching. Large ΔS values occur when macropores are volumetrically dominant yet numerically sparse, resulting in early drainage of large pores while numerous micropores remain water-filled. Spatial analyses show that desaturation proceeds through the nucleation and growth of correlated dry clusters, typically originating in macropore-rich regions and expanding cooperatively as suction increases, leaving behind isolated pockets of trapped water at high suction. This microstructural evolution provides a mechanistic explanation for the shape of the simulated SWCCs and the emergence of hysteresis. Future work may extend the framework to alternative pore-size distributions, three-dimensional lattice representations, contact-angle variability, and direct comparison with microstructural imaging or experimental SWCC data.

6. Declarations

6.1. Author Contributions

Conceptualization, V.G. and J.S.; methodology, V.G. and J.S.; software, V.G. and J.S.; validation V.G. and J.S.; formal analysis, V.G. and J.S; investigation, V.G. and J.S; resources, V.G. and J.S.; writing—original draft preparation, V.G.; writing—review and editing, J.S.; visualization, V.G.; supervision, V.G.; project administration, J.S. All authors have read and agreed to the published version of the manuscript.

6.2. Data Availability Statement

The data presented in this study are available in the article.

6.3. Funding and Acknowledgments

The authors gratefully acknowledge the financial support provided by the Universidad de Nariño and Universidad Mariana. This research was partially funded by the 'Vicerrectoría de Investigaciones e Interacción Social – VIIS' of the Universidad de Nariño, under project number 3523, and Universidad Mariana.

6.4. Conflicts of Interest

The authors declare no conflict of interest.

7. References

[1] Fredlund, D. G., & Anqing Xing. (1994). Equations for the soil-water characteristic curve. Canadian Geotechnical Journal, 31(4), 521–532. doi:10.1139/t94-061.

[2] Fredlund, D. G. (2006). Unsaturated Soil Mechanics in Engineering Practice. Journal of Geotechnical and Geoenvironmental Engineering, 132(3), 286–321. doi:10.1061/(asce)1090-0241(2006)132:3(286).

[3] Rahardjo, H., Kim, Y., & Satyanaga, A. (2019). Role of unsaturated soil mechanics in geotechnical engineering. International Journal of Geo-Engineering, 10(1), 1–23. doi:10.1186/s40703-019-0104-8.

[4] Chang, W. J., Chou, S. H., Huang, H. P., & Chao, C. Y. (2021). Development and verification of coupled hydro-mechanical analysis for rainfall-induced shallow landslides. Engineering Geology, 293, 106337. doi:10.1016/j.enggeo.2021.106337.

[5] Nguyen, T. S., & Likitlersuang, S. (2019). Reliability analysis of unsaturated soil slope stability under infiltration considering hydraulic and shear strength parameters. Bulletin of Engineering Geology and the Environment, 78(8), 5727–5743. doi:10.1007/s10064-019-01513-2.

[6] Vanapalli, S. K., & Oh, W. T. (2010). Mechanics of unsaturated soils for the design of foundation structures. Proceedings of the 3rd WSEAS international conference on Engineering mechanics, structures, engineering geology, 22-24 July, 2010, Corfu Island, Greece.

[7] Yilmazoglu, M. U., & Ozocak, A. (2023). Bearing Capacity of Shallow Foundations on Unsaturated Silty Soils. Applied Sciences (Switzerland), 13(3), 1308. doi:10.3390/app13031308.

[8] Onyelowe, K. C., Mojtahedi, F. F., Azizi, S., Mahdi, H. A., Sujatha, E. R., Ebid, A. M., Darzi, A. G., & Aneke, F. I. (2022). Innovative Overview of SWRC Application in Modeling Geotechnical Engineering Problems. Designs, 6(5), 69. doi:10.3390/designs6050069.

[9] Alnmr, A., Alzawi, M. O., Ray, R., Abdullah, S., & Ibraheem, J. (2024). Experimental Investigation of the Soil-Water Characteristic Curves (SWCC) of Expansive Soil: Effects of Sand Content, Initial Saturation, and Initial Dry Unit Weight. Water (Switzerland), 16(5), 627. doi:10.3390/w16050627.

[10] Pečan, U., Pintar, M., & Kastelec, D. (2023). Variability of in situ soil water retention curves under different tillage systems and growing seasons. Soil and Tillage Research, 233, 105779. doi:10.1016/j.still.2023.105779.

[11] Hohenbrink, T. L., Jackisch, C., Durner, W., Germer, K., Iden, S. C., Kreiselmeier, J., Leuther, F., Metzger, J. C., Naseri, M., & Peters, A. (2023). Soil water retention and hydraulic conductivity measured in a wide saturation range. Earth System Science Data, 15(10), 4417–4432. doi:10.5194/essd-15-4417-2023.

[12] Likos, W. J., Lu, N., & Godt, J. W. (2014). Hysteresis and Uncertainty in Soil Water-Retention Curve Parameters. Journal of Geotechnical and Geoenvironmental Engineering, 140(4), 4013050. doi:10.1061/(asce)gt.1943-5606.0001071.

[13] Kim, J., Hwang, W., & Kim, Y. (2018). Effects of hysteresis on hydro-mechanical behavior of unsaturated soil. Engineering Geology, 245, 1–9. doi:10.1016/j.enggeo.2018.08.004.

[14] Leong, E. C. (2019). Soil-water characteristic curves - Determination, estimation and application. 7th Asia-Pacific Conference on Unsaturated Soils, AP-UNSAT 2019, 7(2), 21–30. doi:10.3208/jgssp.v07.003.

[15] van Genuchten, M. T. (1980). A Closed-form Equation for Predicting the Hydraulic Conductivity of Unsaturated Soils. Soil Science Society of America Journal, 44(5), 892–898. doi:10.2136/sssaj1980.03615995004400050002x.

[16] Vereecken, H., Weynants, M., Javaux, M., Pachepsky, Y., Schaap, M. G., & van Genuchten, M. T. (2010). Using Pedotransfer Functions to Estimate the van Genuchten–Mualem Soil Hydraulic Properties: A Review. Vadose Zone Journal, 9(4), 795–820. doi:10.2136/vzj2010.0045.

[17] Mohajerani, H., Teschemacher, S., & Casper, M. C. (2021). A comparative investigation of various pedotransfer functions and their impact on hydrological simulations. Water (Switzerland), 13(10), 1401. doi:10.3390/w13101401.

[18] Joekar-Niasar, V., & Hassanizadeh, S. M. (2012). Analysis of fundamentals of two-phase flow in porous media using dynamic pore-network models: A review. Critical Reviews in Environmental Science and Technology, 42(18), 1895–1976. doi:10.1080/10643389.2011.574101.

[19] Kanckstedt, M. A., Sheppard, A. P., & Sahimi, M. (2001). Pore network modelling of two-phase flow in porous rock: The effect of correlated heterogeneity. Advances in Water Resources, 24(3–4), 257–277. doi:10.1016/S0309-1708(00)00057-9.

[20] Zaretskiy, Y., Geiger, S., Sorbie, K., & Förster, M. (2010). Efficient flow and transport simulations in reconstructed 3D pore geometries. Advances in Water Resources, 33(12), 1508–1516. doi:10.1016/j.advwatres.2010.08.008.

[21] Nabipour, I., Mohammadzadeh-Shirazi, M., Raoof, A., & Qajar, J. (2025). A Data-Driven Approach for Efficient Prediction of Permeability of Porous Rocks by Combining Multiscale Imaging and Machine Learning. Transport in Porous Media, 152(4), 1–34. doi:10.1007/s11242-025-02167-3.

[22] Showkat, R., Jalal, F. E., & Babu, G. L. S. (2025). Estimation of Soil Water Characteristic Curve Using Machine-Learning Algorithms and Its Application in Embankment Response. Journal of Computing in Civil Engineering, 39(3), 4025012. doi:10.1061/jccee5.cpeng-6062.

[23] Albuquerque, E. A. C., de Faria Borges, L. P., Cavalcante, A. L. B., & Machado, S. L. (2022). Prediction of soil water retention curve based on physical characterization parameters using machine learning. Soils and Rocks, 45(3), 222. doi:10.28927/SR.2022.000222.

[24] Ding, X., & El-Zein, A. (2024). Predicting soil water retention curves using machine learning: A study of model architecture and input variables. Engineering Applications of Artificial Intelligence, 133, 108122. doi:10.1016/j.engappai.2024.108122.

[25] Achieng, K. O. (2019). Modelling of soil moisture retention curve using machine learning techniques: Artificial and deep neural networks vs support vector regression models. Computers and Geosciences, 133, 104320. doi:10.1016/j.cageo.2019.104320.

[26] Zhao, Y., Cui, Y., Zhou, H., Feng, X., & Huang, Z. (2017). Effects of void ratio and grain size distribution on water retention properties of compacted infilled joint soils. Soils and Foundations, 57(1), 50–59. doi:10.1016/j.sandf.2017.01.004.

[27] Kieu, M. T., & Mahler, A. (2018). A study on the relationship between matric suction and the void ratio and moisture content of a compacted unsaturated soil. Periodica Polytechnica Civil Engineering, 62(3), 709–716. doi:10.3311/PPci.11974.

[28] Sethna, J. P., Dahmen, K. A., & Myers, C. R. (2001). Crackling noise. Nature, 410(6825), 242–250. doi:10.1038/35065675.

[29] Illa, X., Rosinberg, M. L., & Vives, E. (2006). Influence of the driving mechanism on the response of systems with a thermal dynamics: The example of the random-field Ising model. Physical Review B - Condensed Matter and Materials Physics, 74(22), 224403. doi:10.1103/PhysRevB.74.224403.

[30] Xu, J., & Louge, M. Y. (2015). Statistical mechanics of unsaturated porous media. Physical Review E, 92(6). doi:10.1103/PhysRevE.92.062405.

[31] Salvat-Pujol, F., Vives, E., & Rosinberg, M. L. (2009). Hysteresis in the T=0 random-field Ising model: Beyond metastable dynamics. Physical Review E - Statistical, Nonlinear, and Soft Matter Physics, 79(6), 61116. doi:10.1103/PhysRevE.79.061116.

[32] Illa, X., & Rosinberg, M. L. (2011). Zero-temperature random field Ising model on a Bethe lattice: Correlation functions along the hysteresis loop. Physical Review B - Condensed Matter and Materials Physics, 84(6), 64443. doi:10.1103/PhysRevB.84.064443.

[33] Rosinberg, M. L., & Munakata, T. (2009). Hysteresis and complexity in the mean-field random-field Ising model: The soft-spin version. Physical Review B - Condensed Matter and Materials Physics, 79(17), 174207. doi:10.1103/PhysRevB.79.174207.

[34] Fytas, N. G., Martín-Mayor, V., Picco, M., & Sourlas, N. (2018). Review of Recent Developments in the Random-Field Ising Model. Journal of Statistical Physics, 172(2), 665–672. doi:10.1007/s10955-018-1955-7.

[35] Gómez, A. V. (2025). A Theoretical Pore Network Model for the Soil–Water Characteristic Curve and Hysteresis in Unsaturated Soils. Civil Engineering Journal (Iran), 11(2), 763–778. doi:10.28991/CEJ-2025-011-02-021.

[36] Rojas, E., & Rojas, F. (2005). Modeling hysteresis of the soil-water characteristic curve. Soils and Foundations, 45(3), 135–145. doi:10.3208/sandf.45.3_135.

[37] Eyo, E. U., Ng'ambi, S., & Abbey, S. J. (2022). An overview of soil–water characteristic curves of stabilised soils and their influential factors. Journal of King Saud University - Engineering Sciences, 34(1), 31–45. doi:10.1016/j.jksues.2020.07.013.

[38] Zhai, Q., Rahardjo, H., & Satyanaga, A. (2018). Uncertainty in the estimation of hysteresis of soil-water characteristic curve. Environmental Geotechnics, 6(4), 204–213. doi:10.1680/jenge.17.00008.

[39] Higo, Y., & Kido, R. (2023). A microscopic interpretation of hysteresis in the water retention curve of sand. Geotechnique. doi:10.1680/jgeot.23.00084.

[40] Mooney, S. J., & Korošak, D. (2009). Using Complex Networks to Model Two- and Three-Dimensional Soil Porous Architecture. Soil Science Society of America Journal, 73(4), 1094–1100. doi:10.2136/sssaj2008.0222.

[41] Mufti, S., & Das, A. (2023). Modeling unsaturated hydraulic conductivity of granular soils using a combined discrete element and pore-network approach. Acta Geotechnica, 18(2), 651–672. doi:10.1007/s11440-022-01597-3.

[42] Zhou, H., Mooney, S. J., & Peng, X. (2017). Bimodal Soil Pore Structure Investigated by a Combined Soil Water Retention Curve and X-Ray Computed Tomography Approach. Soil Science Society of America Journal, 81(6), 1270–1278. doi:10.2136/sssaj2016.10.0338.

[43] Kutílek, M., Jendele, L., & Panayiotopoulos, K. P. (2006). The influence of uniaxial compression upon pore size distribution in bi-modal soils. Soil and Tillage Research, 86(1), 27–37. doi:10.1016/j.still.2005.02.001.

[44] Coppola, A. (2000). Unimodal and Bimodal Descriptions of Hydraulic Properties for Aggregated Soils. Soil Science Society of America Journal, 64(4), 1252–1262. doi:10.2136/sssaj2000.6441252x.

[45] dos Santos Pereira, S. A., Silva Junior, A. C., Mendes, T. A., Gitirana Junior, G. de F. N., & Alves, R. D. (2024). Prediction of Soil–Water Characteristic Curves in Bimodal Tropical Soils Using Artificial Neural Networks. Geotechnical and Geological Engineering, 42(5), 3043–3062. doi:10.1007/s10706-023-02716-x.

[46] Chan, W. K. V. (2013). Theory and applications of Monte Carlo simulations. BoD–Books on Demand, Hamburg, Germany.

[47] Zhou, J., Wang, Y., Qi, P., Ma, R., Vereecken, H., Minasny, B., & Zhang, Y. (2025). Soil Physics-Informed Neural Networks to Estimate Bimodal Soil Hydraulic Properties. Water Resources Research, 61(10), 2024 039337. doi:10.1029/2024WR039337.

[48] Hosseini, R., Kumar, K., & Delenne, J. Y. (2024). Investigating the source of hysteresis in the soil–water characteristic curve using the multiphase lattice Boltzmann method. Acta Geotechnica, 19(11), 7577–7601. doi:10.1007/s11440-024-02295-y.

[49] Wang, J. P., Liu, T. H., Wang, S. H., Luan, J. Y., & Dadda, A. (2023). Investigation of porosity variation on water retention behaviour of unsaturated granular media by using pore scale Micro-CT and lattice Boltzmann method. Journal of Hydrology, 626, 130161. doi:10.1016/j.jhydrol.2023.130161.

[50] Pessoa, T. N., Ferreira, T. R., Pires, L. F., Cooper, M., Uteau, D., Peth, S., Vaz, C. M. P., & Libardi, P. L. (2023). X-ray Microtomography for Investigating Pore Space and Its Relation to Water Retention and Conduction in Highly Weathered Soils. Agriculture (Switzerland), 13(1), 28. doi:10.3390/agriculture13010028.

[51] Pires, L. F., Auler, A. C., Roque, W. L., & Mooney, S. J. (2020). X-ray microtomography analysis of soil pore structure dynamics under wetting and drying cycles. Geoderma, 362, 114103. doi:10.1016/j.geoderma.2019.114103.

[52] Detmann, B. (2025). On several types of hysteresis phenomena appearing in porous media. Mathematics in Engineering, 7(3), 384–405. doi:10.3934/mine.2025016.

[53] Nepal, A., Hidalgo, J. J., Ortín, J., Lunati, I., & Dentz, M. (2025). Mechanisms of interface jumps, pinning and hysteresis during cyclic fluid displacements in an isolated pore. Journal of Colloid and Interface Science, 696, 137767. doi:10.1016/j.jcis.2025.137767.

[54] Lan, Y., Guo, P., Liu, Y., Wang, S., Cao, S., Zhang, J., Sun, W., Qi, D., & Ji, Q. (2024). State of the Art on Relative Permeability Hysteresis in Porous Media: Petroleum Engineering Application. Applied Sciences (Switzerland), 14(11), 4639. doi:10.3390/app14114639.

[55] Kierlik, E., Monson, P. A., Rosinberg, M. L., Sarkisov, L., & Tarjus, G. (2001). Capillary condensation in disordered porous materials: Hysteresis versus equilibrium behavior. Physical Review Letters, 87(5), 55701-1-55701–55704. doi:10.1103/PhysRevLett.87.055701.

[56] Dahmen, K. A., Sethna, J. P., Kuntz, M. C., & Perković, O. (2001). Hysteresis and avalanches: Phase transitions and critical phenomena in driven disordered systems. Journal of Magnetism and Magnetic Materials, 226–230(Part II), 1287–1292. doi:10.1016/S0304-8853(00)00749-6.